Pergamon

Int. J. Heat Mass Transfer. Vol. 37, No. 3, pp. 363–374, 1994

0017–9310/94 $6.00 + 0.00

Convection heat transfer distributions over plates with square ribs from infrared thermography measurements

D. A. ALIAGA, J. P. LAMB and D. E. KLEIN
Department of Mechanical Engineering, The University of Texas at Austin, TX 78712, U.S.A.

(*Received* 25 *January* 1993 *and in final form* 27 *August* 1993)

Abstract—Heat transfer measurements were performed on two ribbed plates, with constant heat flux surfaces, using an infrared (IR) thermography technique. The tests were conducted in a turbulent flow wind tunnel ($0.5 \times 10^6 < Re < 1.5 \times 10^6$) at two roughness heights ($e/D_h = 0.052$ and 0.093). The transverse ribs on the plates had a square cross section. The experimental technique provided local variations of heat transfer coefficients not only between ribs but also surrounding the ribs, with better resolution than techniques currently used. The results suggested a separation–reattachment flow distribution over the plate with a pitch ratio (p/e) of 12 and a trapped vortex flow between ribs for a p/e of 5.

INTRODUCTION

REPEATED ribs are used on heat exchange surfaces to promote turbulence and enhance convective heat transfer. Some applications of augmented heat transfer include fuel rods of gas cooled nuclear reactors, the inside cavities of turbine blades, internal surfaces of pipes used in heat exchangers, and the surfaces of solar collectors.

Numerical simulation of the convection transfer process over rough surfaces is relatively difficult because of limitations on turbulence models. Therefore, numerous experimental investigations have been required to define the effects of many independent parameters. Sparrow and Tao [1] performed experiments using airflow in rectangular ducts ($AR = 6.4$ and 12.8) with one wall roughened. Results suggested that the reattachment distance was insensitive to the pitch variation, but the redevelopment region downstream of reattachment, was substantially lengthened as the pitch increased.

Han [2] determined from experiments in a wind tunnel of square cross section with repeated-ribs on two opposite side walls (while the other two walls were smooth) that, by increasing the relative roughness e/D_h (with constant Reynolds number), both friction factor and Stanton number increased. Also, an increase in Reynolds number caused the average friction factor to approach a constant value while the Stanton number continued to decrease. The average Stanton number of the channel with two ribbed walls was about 1.3 to 2 times that of the completely smooth wall channel. Subsequent tests by Han *et al.* [3] in a similar square duct (p/e varied from 10 to 20, with a constant e/D_h ratio of 0.063) showed that, at $p/e = 10$, the Nusselt number was twice the Nusselt number of a smooth duct. The friction factor in this same case was 4 to 6 times higher. For $p/e = 20$, the results were less impressive with respect to heat transfer enhancement. Tests on a square duct with all walls roughened produced less heat transfer enhancement than the two-roughened-wall duct.

Liou *et al.* [4] used LDV measurements to determine both mean flow and turbulence structure in a wind tunnel ($AR = 2$) which had opposite walls roughened by two square ribs on each wall. Three pitch ratios, 5, 10, and 15, were found to provide different flow characteristics. Results indicated that the reattachment length after the first rib was a weak function of p/e, whereas behind the second rib it was strongly dependent on p/e. The reattachment length increased slightly for a ten-fold increase in Reynolds number. Pressure loss increased with increasing p/e, whereas a p/e of 10 proved to be superior to 5 or 15 with respect to turbulence enhancement.

Hishida and Takase [5] performed experiments with air flowing in a rectangular duct ($AR = 9.4$) having a smooth upper wall and a bottom wall with transverse square ribs. The upper and lower walls of the channel were covered with a stainless steel foil and were electrically heated to provide a constant heat flux boundary. Fully developed and periodic velocity and temperature profiles were attained upstream of the test section. The relative pitch ratio varied from 2.5 to 60. One of the ribs in the test section was independently heated. The ratio of heat flux on this rib to the base heat flux (q''_c/q''_b) was varied from 0.5 to 2.5. Thermocouples of 0.1 mm in diameter were attached to the back of the heating foil to measure the temperature distribution on the plate and the ribs. Experimental variations of local Nusselt number over the rib surface were determined.

Flow visualization experiments performed at a pitch ratio of 10 showed that a turbulent recirculating flow was formed in the wake behind the rib. With the vortex shedding from the rib, the oblique air stream

NOMENCLATURE

AR	aspect ratio. Width to height of duct cross section
D_h	hydraulic diameter
e	height of roughness element
f	friction factor
h, HTC	convection heat transfer coefficient
k	thermal conductivity
K_1, K_2	experimental constants in equation (1)
Nu	Nusselt number
p	roughness pitch
q''	heat flux
Re	Reynolds number based on V_c and D_h
S	signal measured by the infrared system
T_{bulk}	bulk temperature of surrounding air
V_c	centerline velocity
X	position along ribbed plate.

Greek symbols

ε	emittance
τ	absorptance.

Subscripts

cond	conduction
elec	generated using electric power
rad	radiation
r	reference
o	object or target.

impinged on the base surface in an oscillatory pattern, producing a fluctuating reattachment region. The overall Nusselt number of the whole ribbed surface increased with increasing q''_e/q''_b for pitch ratios less than 10.

Liou and Hwang [6] performed friction and heat transfer measurements for fully developed channel flow ($AR = 4$) with two rib-roughened opposite walls and pitch ratios of 10, 15 and 20. Temperature measurements were made using both a laser holographic interferometer and thermocouples. Results indicated that, at a constant Reynolds number, friction factor and Nusselt number increased with increasing roughness height ratio, whereas these parameters decreased with increasing pitch for a constant rib height. The length of the separation bubble behind the rib did not change as the pitch increased, while the distance between the reattachment point and the following rib increased with pitch. It was shown that there is an optimum pitch ratio for maximum overall heat transfer enhancement.

Experimental studies of heat transfer over rough surfaces using infrared thermography are very limited [7]. However, with recent developments in image resolution, optical attachments, detector cooling devices, as well as software and computer capabilities, infrared thermography has gained recognition as an appropriate research tool in the area of heat transfer. In the present investigation, an experimental technique was developed to study the heat transfer over surfaces with repeated-rib-roughness and constant heat flux placed in a subsonic wind tunnel. The objective was to obtain accurate measurements of heat transfer coefficients not only on the heated base surface but also on the ribs. This was accomplished by using an infrared camera and reference thermocouples attached to the rough surfaces. Thin stainless steel foils attached to the ribbed surface and heated electrically were used to achieve a constant heat flux boundary condition. The combination of infrared thermography and heating foil technique applied to the study of rough flow makes the present experimental method unique and superior with respect to the previously developed methods noted earlier.

EXPERIMENTAL EQUIPMENT

Wind tunnel

An open circuit tunnel, with a total length of 24 m, was operated within a Reynolds number range of 0.5×10^6 to 1.5×10^6. The forced draft fan was driven by a 75 kW electric motor. The interior cross section of the tunnel had a constant width of 1.14 m but the height could be varied from 0.1524 to 0.3810 m (varying the AR of the duct from 7.2 to 2.9). Ribbed plates were installed inside the test section and placed on the bottom wall of the wind tunnel as shown in Fig. 1(a).

Test section and plates

Six openings of 76×305 mm were cut on the roof of the test section to allow the IR camera to scan the test plate (Fig. 1(a)). A pitot tube supported by a traverse Compumotor system was used to determine velocity profiles across the channel. An infrared camera (Inframetrics) was attached to a rail system so it could move over the test section and scan the plate surface through the openings located on the roof (Fig. 1(a)). Pressure ports on the roof of the tunnel were used to measure static pressure drop along the tunnel. Below the test plate, a layer of fiberglass insulation 152 mm thick minimized heat losses.

Two plates with ribs of square cross section were built using 19 mm thick plywood. The test plates had a length of 1.83 m and a width of 1.105 m. The plates included square ribs of $e = 25$ mm (Fig. 1(b)). The plate with $p/e = 12$ had six ribs while the second plate ($p/e = 5$) has 14 ribs. These two values of pitch were selected so as to produce entirely different flow patterns between ribs. The top and bottom surfaces of

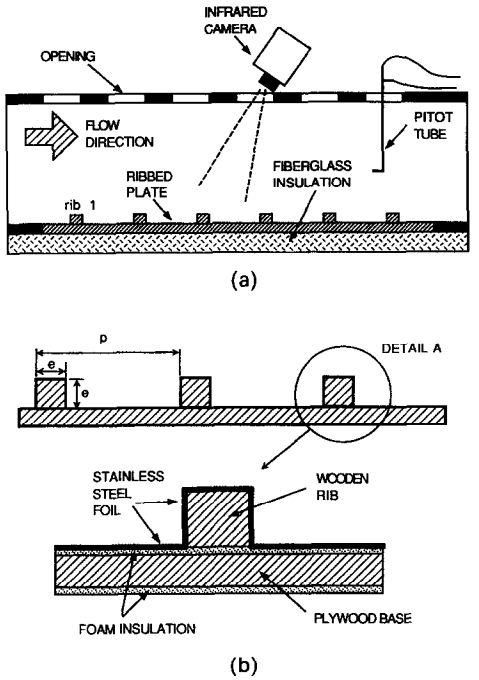

FIG. 1. (a) Ribbed plate inside test section of wind tunnel. (b) Characteristic dimensions of test plate with detail of construction materials for ribbed plate.

the plates were covered by 3 mm thick foam insulation ($k = 0.03$ W m^{-1} K^{-1}) as shown in detail A of Fig. 1(b).

Fifteen strips of stainless steel foil 20 mm wide and 0.0254 mm thick were glued to the top surface of the ribbed plates. These foils extended over the entire length of the test plate, covering an area 315 mm wide in the center of the plate. The foils were connected in series and heated through a variable transformer bank. Assuming uniform electrical resistance in the foils and constant heat losses through the bottom of the plates, a nearly constant heat flux surface was created. The surface of the stainless steel foils was coated with black paint (Krylon) to maximize its surface emittance.

Data acquisition instrumentation

Instrumentation included a 2.2 kPa differential pressure transducer (Valydine) to measure pressure drops along the wind tunnel, a Digital Multimeter (Keithley) to measure voltages from the thermocouples, a pitot tube and traveling system (Compumotor), an IBM PC-XT, and a model 600L infrared system (Inframetrics).

The 600L IR system has a square shape (side of length = 0.025 mm) Mercury–Cadmium–Telluride (Hg–Cd–Te) detector with a specified time constant of 0.5–1 μs and operates in the 8–12 μm infrared waveband [8]. This infrared detector is cooled to 77 K by a closed cycle microcooler. Unlike infrared cameras that use liquid nitrogen cooling, the model 600L can operate continuously and can be positioned at any angle with respect to the target surface.

Resolution and uncertainty of infrared measurements

Thermal resolution in the 600L model is specified according to either of two parameters: NETD or MDTD [9]. The NETD (noise equivalent temperature difference) is defined as the temperature difference which produces a change in signal output equal to the system r.m.s. noise. The NETD in the model 600L system at 30°C is less than 0.2°C. The MDTD (minimum detectable temperature difference) performance criterion considers the effect of the eye's persistence and camera frame rate. The MDTD for the model 600L at 30°C is 0.1°C.

Calibration tests were performed to determine the accuracy, spatial resolution, emittance variation, response to temperature gradients, and effect of surroundings on the infrared measurements. Reference thermocouples placed at strategic locations over the ribbed plates were used to correct temperature readings of the infrared system in order to minimize measurement errors. Details of this procedure are given in refs. [10, 11].

The signal measured (S_i) by the infrared detector due to radiation from the i-surface (object) with emittance ε_i, absorptance τ of the medium between the surface and detector (neglecting atmospheric radiation), and reflected radiation from an adjacent j-surface (surroundings) can be approximated as

$$S_i = \varepsilon_i \tau \frac{K_1}{\left[\exp\left(\frac{K_2}{T_i}\right) - 1\right]} + \tau(1-\varepsilon_i)S(T_j) \quad (1)$$

where the subscript $i \equiv$ 'o' for object and 'r' for reference.

Equation (1) considers the approximations of gray body and Lambertian surface. A simultaneous measurement on a target area of the heating foil surface and on a reference foil thermocouple placed in the same field of view of the target area will give S_o and S_r in equation (1). Then, using the two equations, a solution for the object (target) temperature (T_o) can be found [10–12]. Since both the target and reference surfaces were submitted to the same reflected radiation from the surroundings (j-surface), and their emittance was the same (both surfaces were coated with the same type of paint), the effect of the surrounding radiation ($S(T_j)$) cancels out.

From the Kline–McKlintock [13] calculations, the uncertainty for the T_o measurements was ± 0.3°C maximum. This relatively small value indicates that the present method can produce accurate results.

The conversion of the temperature to heat transfer coefficient was calculated using the following equation

$$h = \frac{[q''_{\text{elec}} - q''_{\text{cond}} - q''_{\text{rad}}]}{[T_o - T_{\text{bulk}}]}. \quad (2)$$

The recorded variation of T_{bulk} from the entrance to the exit of the test section was negligible (less than 0.5°C) and therefore, the entrance temperature to the

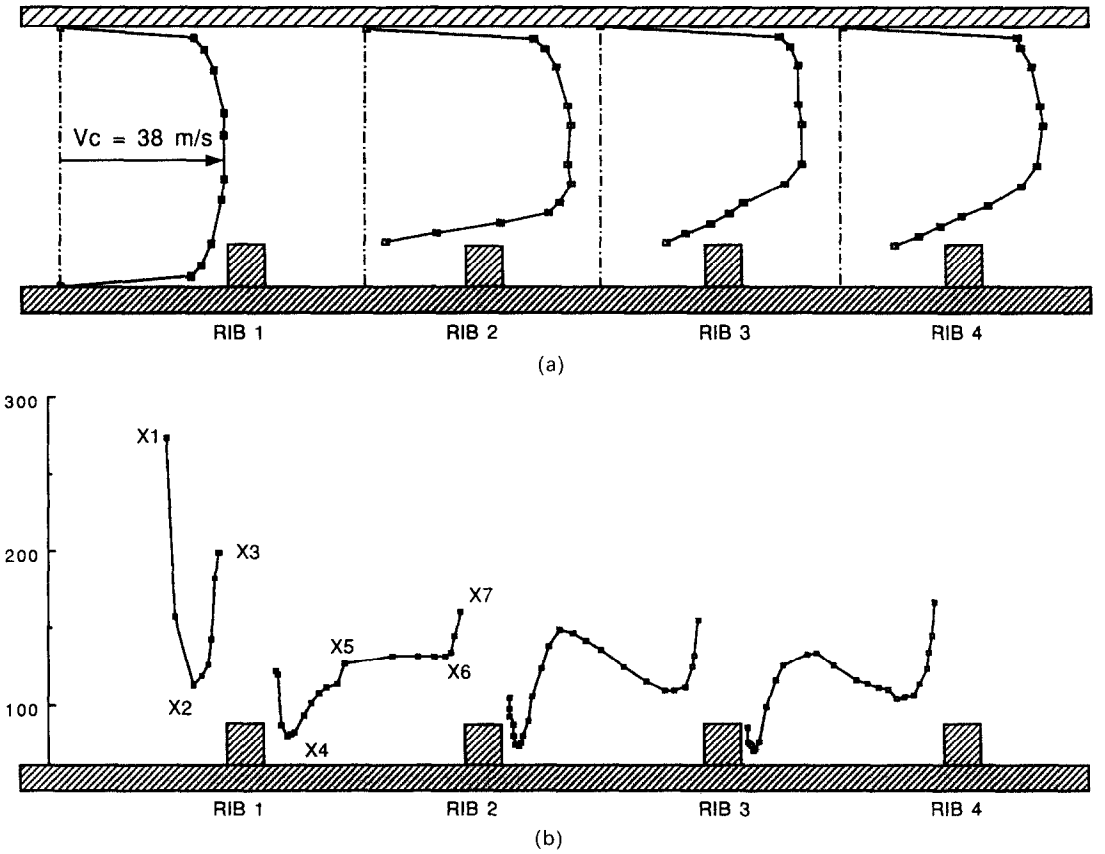

FIG. 2. (a) Mean velocity profiles in test section of wind tunnel (Re = 1.5 E+6, p/e = 12). (b) Local heat transfer coefficient distributions along test plate (Re = 1.5 E+6, p/e = 12).

test section was assumed constant. Conduction losses through the bottom of the plate determined from the readings of heat flux gages were estimated to be an average 2% of the heat input. The heat losses by radiation were 5% of the electric power into the plate. The total uncertainty of the heat transfer coefficient from equation (2) was $\pm 8\%$. The uncertainty of the HTC considering only the temperature uncertainty T_0 (case of measurements performed in an area next to a reference thermocouple) was less than $\pm 5\%$. Additional information about the IR measuring technique is found in refs. [10, 11].

RESULTS AND DISCUSSION

Flow and thermal development

Velocity profiles taken with a pitot tube midway between ribs for the plate with $p/e = 12$ are shown in Fig. 2(a) and confirm that the flow was developing hydraulically. The similarity of the last two velocity profiles indicates that the flow had reached fully developed conditions after the third rib. Figure 2(b) shows the heat transfer coefficient (HTC) distributions between ribs at the base of the test plate for $p/e = 12$. Only the local HTC distributions between ribs 2 and 3 and between subsequent ribs are similar.

The maximum HTC (269 W m^{-2} K^{-1}) for the entire base surface of the test plate occurs upstream of rib 1 (X1 in Fig. 2(b)). Further downstream the HTC decreased to a minimum value at X2 where part of the flow separated from the base surface to pass over the rib. At X3 a secondary peak value of HTC occurred. This point was within a separated vortex at the base of rib 1 but was influenced by the impingement of the main flow at the front face. Between ribs 1 and 2 the local HTC distribution showed a minimum at point X4 which was also within a separated vortex. The maximum HTC was 164 W m^{-2} K^{-1} at point X7 which, like X3, was related to impingement on the front face. The absence of a peak value in this region suggests that there may be no clear reattachment–separation pattern but rather a thinning of the vortex trapped between the two ribs. This can be inferred from the nearly constant value of HTC between X5 and X6.

As in the case of $p/e = 12$, the velocity profiles indicate fully developed conditions after the third rib (Fig. 3(a)) and the distributions of HTC between ribs (Fig. 3(b)) become similar after the second rib for the test plate with $p/e = 5$. At the beginning of the test plate (point X1) and at the bottom of the front face of rib 1 (point X3) a maximum HTC of 145 W m^{-2} K^{-1}

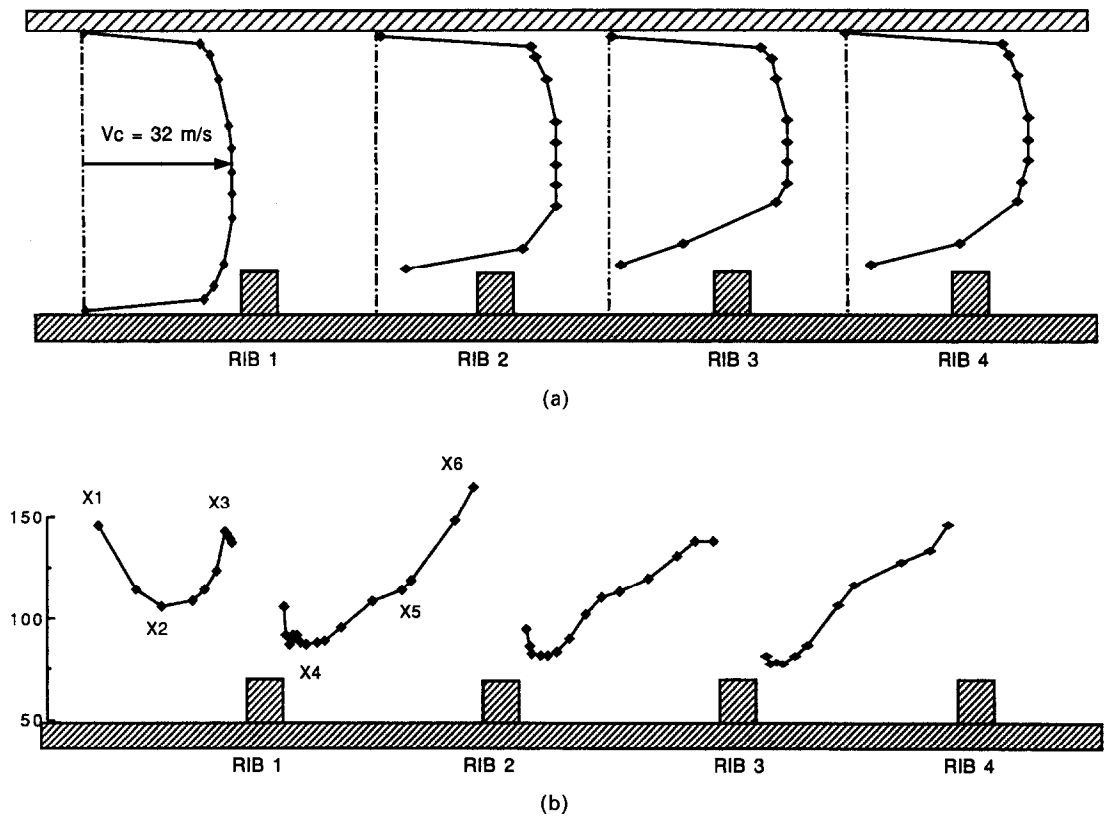

FIG. 3. (a) Mean velocity profiles in test section of wind tunnel (Re = 1.0 E+6, p/e = 5). (b) Local heat transfer coefficient distributions along test plate (Re = 1.0 E+6, p/e = 5).

was measured. A minimum *HTC* of 106 W m^{-2} K^{-1} occurred at point X2 (separation location). The local *HTC* distribution between ribs 1 and 2 showed a steep increase with a minimum of 73 W m^{-2} K^{-1} at point X4 and a maximum of 161 W m^{-2} K^{-1} at point X6. At point X5, there was a slight change in the slope of the variation. It is seen that the distributions of local *HTC* between ribs 2 and 3 and between 3 and 4, were generally similar to that between ribs 1 and 2 (Fig. 3(b)). This was not true for p/e = 12 (Fig. 2(b)).

Figures 4(a), (c), and (e) show local *HTC* distributions for the first three ribs in the case of p/e = 12 while Figs. 4(b), (d) and (f) present possible flow distributions for each rib. The distributions of *HTC* on the first two ribs are quite different from subsequent ribs, indicating that the flow is developing. After the second rib the distributions of *HTC* are generally similar. The *HTC* distributions surrounding the first and second ribs (Figs. 4(a) and (c)) show that the ratio of the *HTC* at X/e = 1 (top upstream corner of rib) to the *HTC* at X/e = 0 (bottom of rib) was approximately 2. At the third rib, this ratio dropped to 1.56. This is probably due to a higher impingement velocity near the front face of the first two ribs (Figs. 4(b) and (d)). As the flow passes the second rib, it establishes a regular pattern of separation and reattachment. The values of the *HTC* distribution surrounding the back face of the first rib are higher than for subsequent ribs. This variation suggests the presence of a smaller recirculating vortex behind the first rib as compared with subsequent ribs (Figs. 4(b), (d) and (f)).

The *HTC* distributions on the top surfaces of the first three ribs for p/e = 12 are noticeably different from each other. The *HTC* distribution over the top surface of the first rib (Fig. 4(a)) indicates a possible separation–reattachment–separation pattern (Fig. 4(b)) which can also be inferred from the distributions at the corners (X/e = 1 and 2). The *HTC* distribution on the top surface of the second rib (Fig. 4(c)) is characteristic of boundary layer growth (Fig. 5(d)) which suggests very little effect of separation at the front corner. The *HTC* distribution on the top surface of the third rib (Fig. 4(c)) also suggests a region of separation–reattachment–separation of flow (Fig. 4(f)) but with a larger region of attached flow than for the first rib (in view of the larger *HTC* values on the top surface of rib 3).

Figures 5(a), (c), and (e) show the local *HTC* distribution for the first three ribs in the case of p/e = 5. As with the case of p/e = 12, the distributions of *HTC* surrounding the first ribs indicated that the flow was developing. In contrast to the p/e = 12 case, the ratio of maximum (at the top corner) to minimum (at the

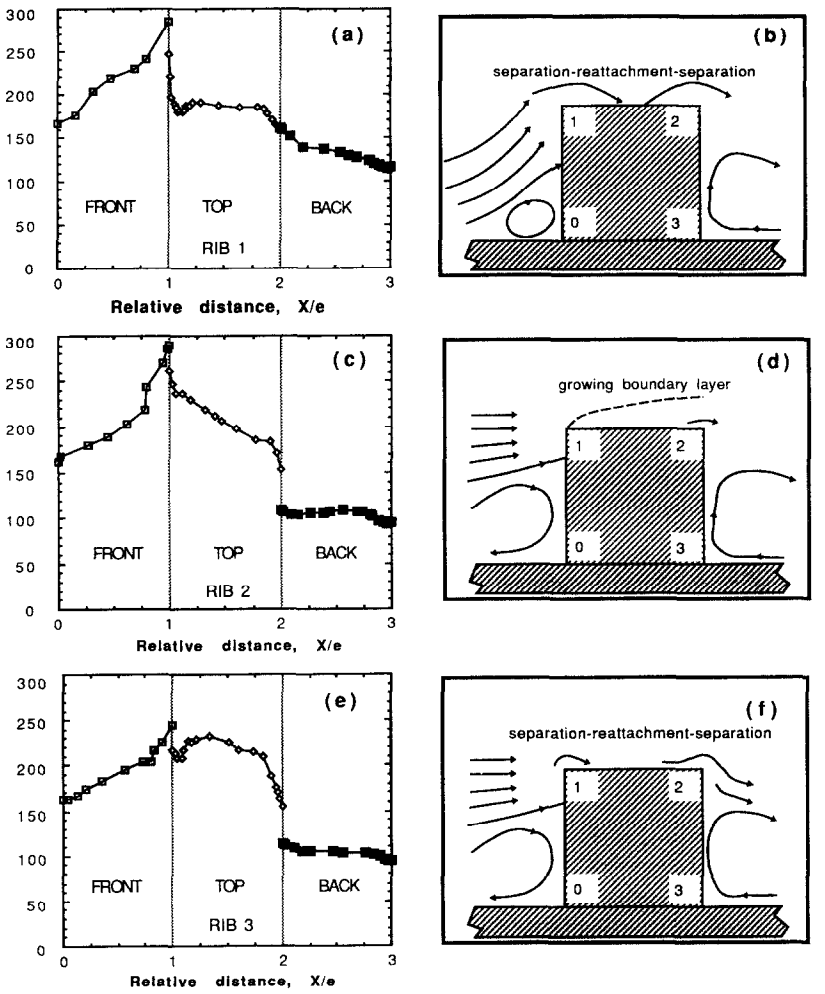

FIG. 4. Variation of heat transfer coefficient and possible flow distributions around first three ribs (Re = 1.5 E+6, p/e = 12).

bottom) HTC on all of the three front surfaces of the ribs was approximately 1.5. The HTC variation on the front face increased monotonically, indicating a region of reattachment near the top of the rib. The HTC distribution on the top face of rib 1 shows a possible region of separation–reattachment–separation (Fig. 5(b)). This is the only section of the plate where such a region was observed. The distribution of the local HTC in the back face of rib 1 shows a decreasing trend with maximum at the top corner of the back surface. The maximum local HTC at the back surface of rib 1 was greater than for subsequent ribs (Figs. 5(a), (c), and (e)). This could be caused by a smaller vortex (therefore higher velocities) behind the first rib as opposed to a larger recirculating flow behind the subsequent ribs as shown schematically in Figs. 5(b), (d), and (f). The local HTC distribution on the top surface of rib 2 (Fig. 5(c)) decreases monotonically with no apparent region of reattachment indicating a possible pattern of boundary layer growth. At the downstream corner of this surface, a nonlinear trend develops indicating a possible region of separation (Fig. 5(d)).

Figure 5(e) shows the local HTC distribution surrounding rib 3. At this point, a similarity between the distribution on the third rib and subsequent ribs has appeared, indicating a repeated pattern of flow. The increasing trend of the HTC from bottom to top of the front face of rib 3 indicates a reattachment of the primary flow on this front face. The HTC distribution on the top of rib 3 decreases monotonically from the upstream corner towards the downstream corner. The nonlinear trend observed in previous ribs does not occur at the downstream corner, indicating there is no local separation. A comparison of the HTC distributions on ribs 2 and 3 for the two values of p/e shows clearly that the trapped vortex between ribs (p/e = 5) allows the outer flow to pass over the ribs with very little deflection as compared with the flow patterns suggested for p/e = 12.

A comparison of the local HTC distribution surrounding rib 3 (Figs. 4(e) and 5(e)) for the two test

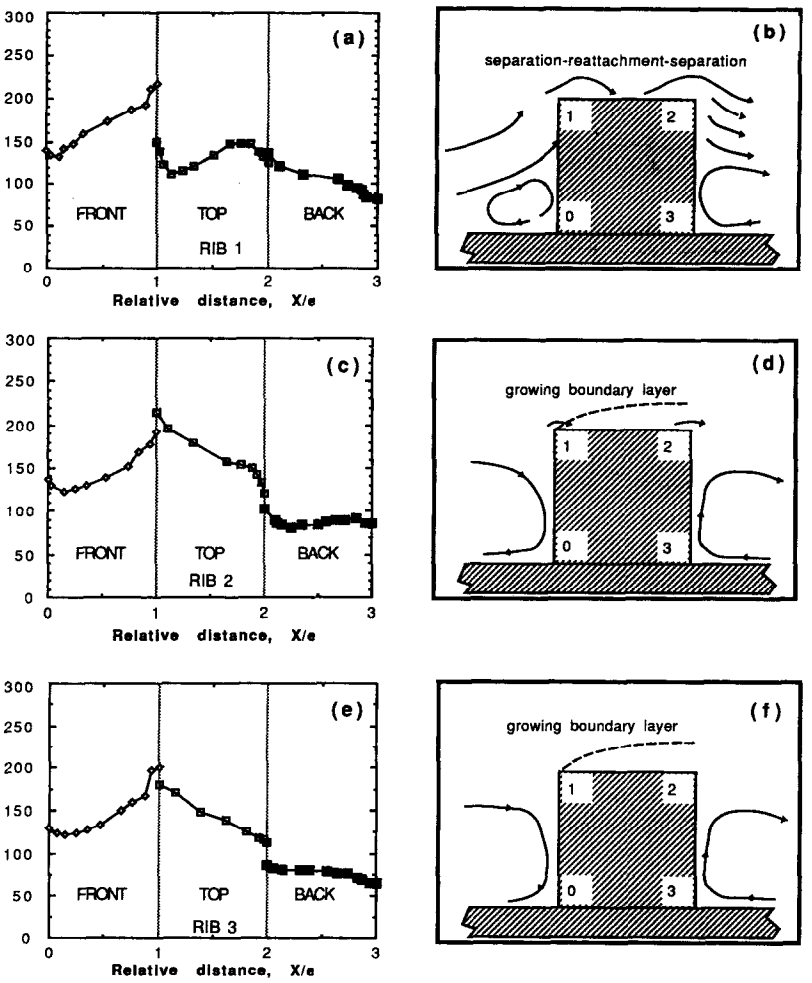

FIG. 5. Variation of heat transfer coefficient and possible flow distributions around first three ribs (Re = 1.0 E+6, p/e = 5).

plates indicates that the front and back *HTC* distributions are similar for the two pitch ratios whereas, on the top of the rib, the *HTC* distribution of the higher pitch had a maximum value at the middle of the rib and decreased towards upstream and downstream corners. In contrast, for the lower pitch ratio the maximum *HTC* occurred at the upstream corner of the rib and then decreased monotonically towards the downstream corner. The different flow patterns which produced these two types of distributions were discussed in conjunction with Figs. 4(f) and 5(f).

In contrast to the differences between the *HTC* distributions for the two values of p/e considered, the average *HTC* distributions over both plates were similar. Figure 6(a) shows the trend of the average *HTC* for $p/e = 12$. The largest average *HTC* at the base surface occurs upstream of the first rib (156 W m^{-2} K^{-1}) as one would expect. After the first rib, the standard deviation of the average *HTC*s between ribs was 3%. Since the uncertainty of the *HTC* is 5% [10, 11], the average base *HTC* after the first rib can be considered constant. The average *HTC* at the front and back of the ribs was the highest at the first rib. The maximum average *HTC* at the front face of the first rib was due to the direct impingement on this surface. The average *HTC* (front surface) decreased for subsequent ribs because of the blockage effect which reduced the average velocity between ribs and also because of the growth of the boundary layer on the base surface. The average *HTC* on the rear face of the first rib was somewhat larger than for subsequent ribs due possibly to higher wake velocities behind the first rib than for subsequent ribs because of the general dissipation of mechanical energy by turbulence. Therefore, the typical residence time of the fluid behind the first rib will be less than for the following ribs. A comparison of Figs. 6(a) and (b) shows that an increase in the relative roughness (from 0.052 to 0.093) produced a relatively large increase in the average *HTC* distribution on the top surfaces of the ribs for the plate with $p/e = 12$. In contrast, the plate with $p/e = 5$ did not show any significant increase in the average *HTC* (top surface) due to relative roughness change.

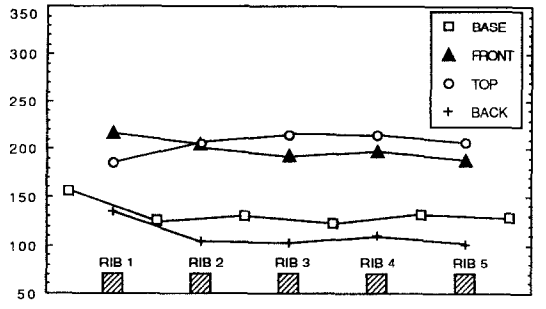

(a)

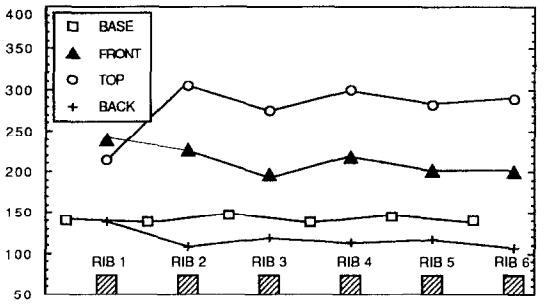

(b)

FIG. 6. (a) Average *HTC* distribution on plate with $p/e = 12$ ($e/D_h = 0.052$, $Re = 1.5$ E+6). (b) Average *HTC* distribution on plate with $p/e = 12$ ($e/D_h = 0.093$, $Re = 0.7$ E+6).

Local heat transfer coefficients between ribs

Figure 7(a) shows the local *HTC* distribution between ribs 5 and 6 in the region of the plate where similar patterns of *HTC* distribution occur. A minimum *HTC* occurs at point X8 (behind the rib) due to the recirculating flow whereas a local maximum *HTC* value occurs at point X9 due to the flow reattachment point. In the similarity region (downstream of rib 3) the distance from the back face of a rib to the reattachment point was determined to lie between three to four rib heights. A decrease of the local *HTC* after reattachment continued until a minimum *HTC* occurred at X10 due to flow separation. The distance from the separation point to the downstream rib was about one to two rib heights. That part of the flow trapped within a small vortex at the base of the rib is thought to produce the maximum local *HTC* shown at X11. This variation was also found in naphthalene tests performed previously [1].

Flow visualization tests performed using yarn tufts indicated that flow reattachment occurred at the position marked by line B–B′ (Fig. 7(a)) confirming the results from the IR measurements. Another flow visualization test using a mixture of water and corn starch applied to the plate showed that there are two regions where the water mixture was relatively stagnant (indicating a very low speed vortex). The first region was between rib 5 and line A–A′. The second region was between rib 6 and line C–C′.

For the plate with $p/e = 5$, the local *HTC* distribution between ribs 3 and 4 (Fig. 7(b)) is representative of *HTC* distributions subsequent to rib 2. This *HTC* distribution suggests a trapped vortex between ribs. The downstream end of the vortex (region A) produces a thinner boundary layer on the base surface (thus higher values of h). At the upstream end (region B), there is probably a secondary vortex (C) which slightly enhances the heat transfer. Also, no region of reattachment (as in the case $p/e = 12$) occurs between the closely spaced ribs. Flow visualization tests using the water–starch mixture showed a relative stagnant film between rib 3 and line D–D′ where lower *HTC* values (and lower fluid velocities) occurred. In contrast, the water film applied initially was wiped away by the higher velocities existing between line D–D′ and rib 4.

Figure 8 shows the effects of Reynolds number and relative roughness on the *HTC* distribution between ribs. In Fig. 8(a), it is seen that an increase in the Reynolds number of 50% produced a uniform increase of about 10% in the *HTC* distribution. The same type of uniform increase in the *HTC* distribution occurred in the case of an increase of the relative roughness height (Fig. 8(b)). A 20% increase in the local *HTC* was produced by a doubling of the relative roughness.

The effect of an increase in the Reynolds number on the HTC distribution between ribs with $p/e = 5$ is shown in Fig. 9(a). The *HTC* distributions show that a 50% increase in the Reynolds number produced an increase in both the value of *HTC* and average slope of the *HTC* distribution between ribs. A relatively higher *HTC* increase occurred near rib 4 than behind rib 3 where a more stagnant flow exists. Figure 9(b) shows that an increase in relative roughness produced a larger increase in the local *HTC* near rib 4. Behind rib 3, where the vortex boundary layer is thickest, the increase in the relative roughness height produced no heat transfer enhancement.

Heat transfer coefficients surrounding ribs

Figure 10 shows the average *HTC* distribution surrounding rib 4 for two pitch ratios ($p/e = 5$ and 12) and two Reynolds numbers. At the low Reynolds number ($Re = 1.0 \times 10^6$), the average *HTC* values of the higher pitch plate ($p/e = 12$) were greater than the lower pitch plate. When the Reynolds number was increased to 1.5×10^6, the situation was reversed. This result suggests that the benefits of heat transfer enhancement are dependent on both Reynolds number and pitch ratio.

Figure 11(a) shows the local *HTC* distribution surrounding rib 4 at two different Reynolds numbers for $p/e = 12$. The increase in local *HTC* was highest at the top of the rib and lowest at its back surface which is adjacent to a vortex flow. Therefore, Reynolds number affects primarily the front and top convection rates. Figure 11(b) shows the local *HTC* distribution surrounding rib 4 at two different relative roughness

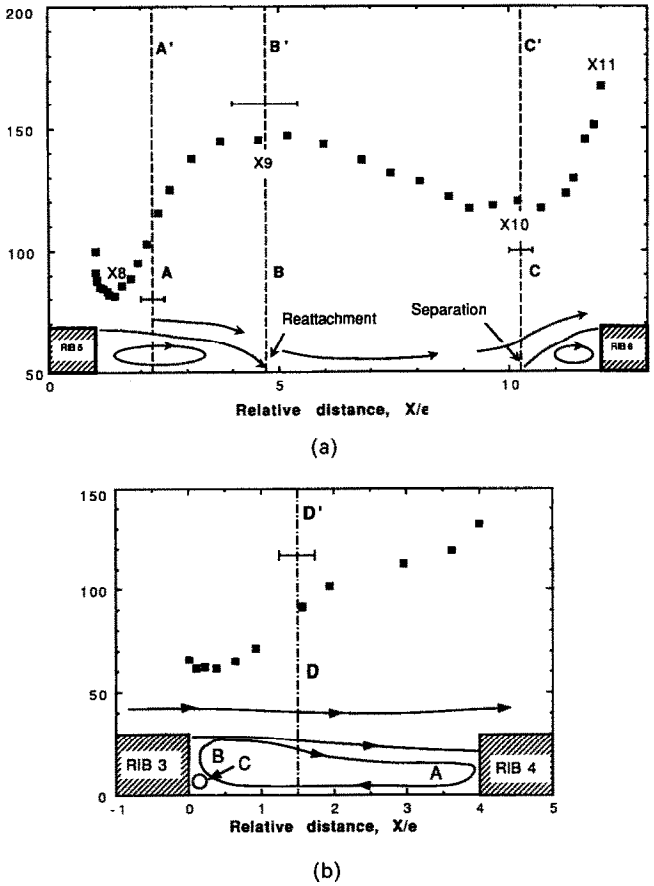

FIG. 7. (a) Local *HTC* distribution and flow visualization results indicative of flow with recirculation and reattachment regions on test plate with $p/e = 12$ ($Re = 1.5\,E+6$, $e/D_h = 0.052$). (b) Local *HTC* distribution and flow visualization results indicative of recirculating flow on test plate with $p/e = 5$ ($Re = 1.0\,E+6$, $e/D_h = 0.052$).

heights for $p/e = 12$. The highest heat transfer enhancement occurred on top of the rib due to the increase in the average flow velocity over the higher rib. The surface least affected by the relative roughness increase was the back of the rib because the vortex pattern was also relatively unaffected.

Figure 12(a) shows a comparison of the local *HTC* distribution surrounding rib 4 at two different Reynolds numbers for $p/e = 5$. An increase in the Reynolds number caused a greater increase in the front and top faces of the rib than on the back face of the rib where the recirculating flow is strongest. In addition, the slope of the local *HTC* distribution on the top face of the rib increased slightly. Figure 12(b) shows that an increase of relative roughness height produced an increase in local *HTC* at the top surface of rib 4 ($p/e = 5$). This occurred because the trapped vortices at the front and back of the rib act as insulating regions which prevented the main flow from affecting the base region (see Fig. 11(b)).

Static pressure distribution and friction factors

In the smooth wall section of the wind tunnel, the pressure distribution decreased linearly as expected. The mean static pressure distribution in this section gave correlation coefficient values of 0.99 or higher. As the flow entered the ribbed test section, the static pressure dropped steeply and nonlinearly during the developing region. Farther downstream, the static pressure recovered and then again began to decrease linearly, indicating that some mean flow stabilization had been achieved. This linear pressure decay occurred approximately between the third and sixth ribs. The value of the correlation coefficient for the mean pressure distribution between these ribs was not as high (≈ 0.9) as correlation coefficients obtained with pressure data from the smooth section. This is attributed to the turbulent disturbances caused by the rough flow.

The ratio of rough to smooth friction factor was between 5 and 10. No variation of friction factor with Reynolds number was found except in the case of tests with high roughness height, where the friction factor in the smooth section decreased from 0.02 to 0.01 with an increase in the Reynolds number for a plate with $p/e = 12$. In the case of $p/e = 5$ with high roughness height, the friction factor in the smooth and rough sections increased from 0.01 to 0.02, and 0.1 to 0.2, respectively, with an increase in the Reynolds number.

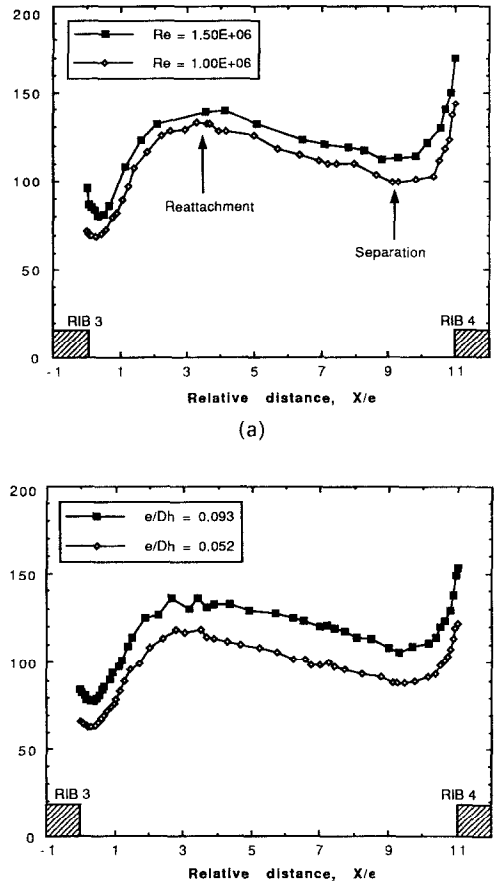

FIG. 8. (a) Effect of the Reynolds number on the *HTC* at the base surface ($p/e = 12$). (b) Effect of the relative roughness on the *HTC* at the base surface ($p/e = 12$).

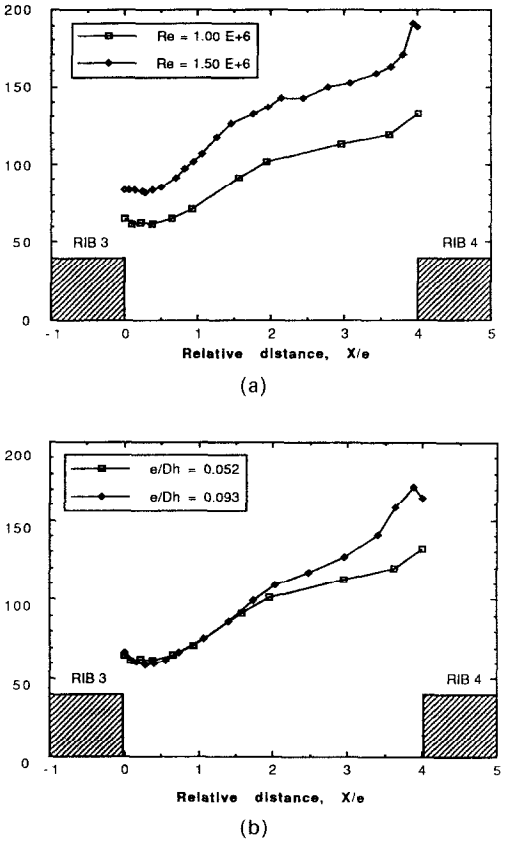

FIG. 9. (a) Effect of the Reynolds number on the *HTC* at the base surface ($p/e = 5$). (b) Effect of the relative roughness on the *HTC* at the base surface ($p/e = 5$).

CONCLUDING REMARKS

Results of the present investigation have demonstrated the excellent capabilities of an infrared measurement technique for obtaining detailed distributions of heat transfer coefficient on a complex surface, capturing variations in the convection heat transfer rate due to the occurrence of reattachment, recirculation and separation. The IR detector's microcooler allowed the system to operate continually with no restrictions on camera position as occurred with previous liquid nitrogen cooled IR cameras. The camera could be pointed directly at a surface and thus one did not require mirrors or reflective optics which would increase errors due to transmittance effects. The effects of IR camera vibration under flowing conditions in the wind tunnel were minimized with the use of proper software to average sequential thermal images and thus produce a sharp, thermal image. The use of a zoom lens increased the spatial resolution of the IR camera and allowed one to obtain greater detail of the temperature distributions around ribs. The fast response of the IR detector (order of 1 μs) produced a 'real time' view of the ribbed surfaces under study which allowed one to observe the transient motions near flow reattachment, confirming that this process does not occur at a fixed location but oscillates through a 'region' of reattachment.

The IR system eliminated the need for a large array of thermocouples to obtain a detailed spatial distribution of temperature on the ribbed surfaces. A few reference thermocouples placed on the test plates provided a satisfactory way of minimizing and controlling errors in readings of the infrared system, and created a minimum disturbance of the surface heat flux at the test plate.

The wood and foam materials used to build the test plates were both inexpensive and good insulators. A maximum of only 6% of the total heat generated was lost by conduction through the plates. Under forced convection conditions, heat losses at the edges of the foils were not significant. This was probably due to (1) the small thickness of the foil, (2) the small separation between foils (1–1.5 mm), and (3) the alignment of foils with the main flow direction. The time response of the electrically heated surfaces (stainless steel foils) to the electric power applied was relative fast (order of seconds). However, the time for the whole system (wood, foam, and stainless steel foil) to achieve steady state was between 1 and 2 h. The heating foils provided a constant surface heat flux condition on the test plates,

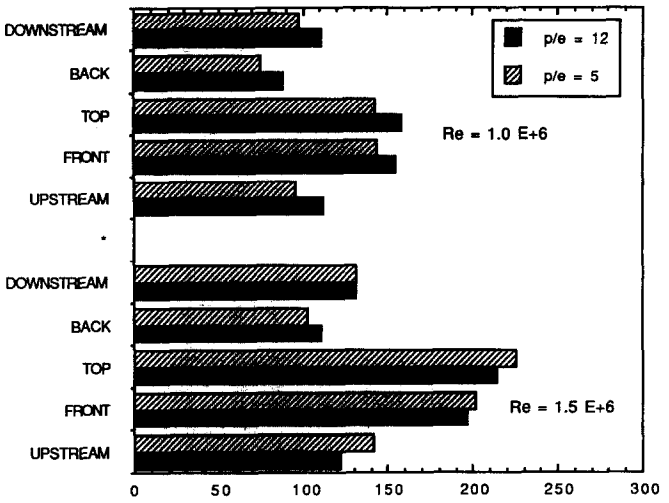

FIG. 10. Effect of the Reynolds number on the average *HTC* surrounding rib 4 at two pitch ratios.

and permitted a direct correlation between surface temperature and heat transfer coefficient. At regions of reattachment, low temperatures were achieved, giving values of heat transfer coefficient values. Conversely, at regions of separation and recirculation, the opposite effect occurred.

After the second rib on the test plates, the heat transfer coefficient distributions on the rib surfaces, as well as the base surface between ribs, were found to be similar. Velocity profiles along the test section also showed similarity after the second rib. For three groups of surfaces (base between ribs, front and rear

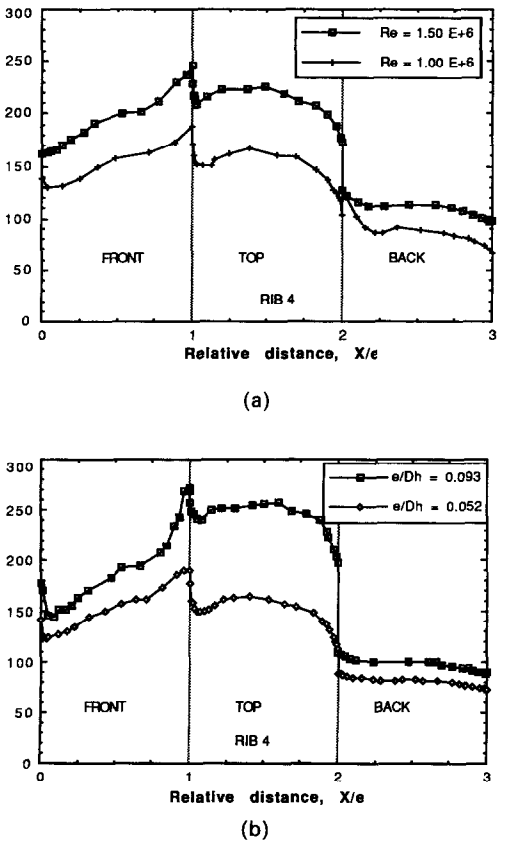

FIG. 11. (a) Effect of Reynolds number on the local *HTC* surrounding rib 4 ($p/e = 12$). (b) Effect of relative roughness on the local *HTC* surrounding rib 4 ($p/e = 12$).

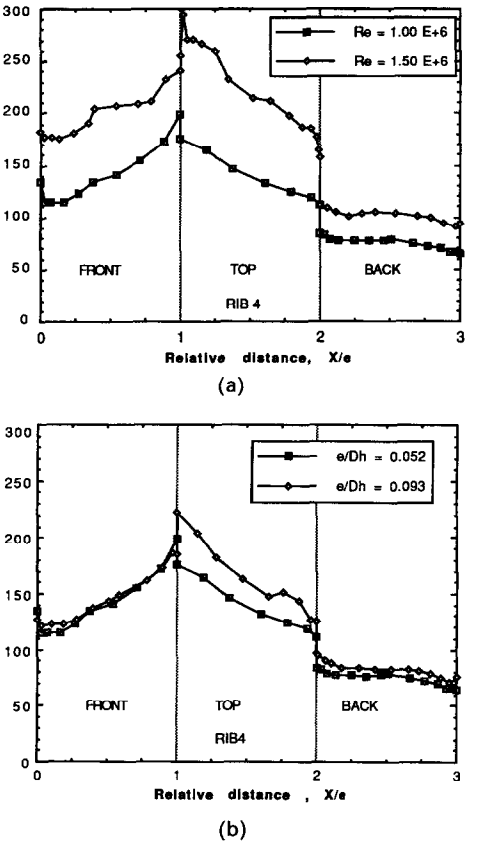

FIG. 12. (a) Effect of Reynolds number on the local *HTC* surrounding rib 4 ($p/e = 5$). (b) Effect of relative roughness on the local *HTC* surrounding rib 4 ($p/e = 5$).

surfaces of the ribs) of the test plates, the average *HTC* exhibited a decreasing trend away from the leading edge. In contrast, *HTC* values on the top surfaces of the ribs showed an increasing trend at the leading edge, becoming nearly constant downstream. The difference of the top surface average *HTC* minus the front surface average *HTC* on the ribs increased with increasing e/D_h. This increase was higher for the plate with $p/e = 12$, than for the plate with $p/e = 5$, indicating that the former is more sensitive to channel height variations.

The local *HTC* distribution over the plate with $p/e = 12$ suggested a flow pattern which included both reattachment and recirculation. A relatively high value of the *HTC* occurred at the reattachment point. Nevertheless, this *HTC* value was not necessarily the maximum since immediately upstream of the rib another high value of the *HTC* occurred which is attributed to a vortex near the rib. The location of flow reattachment was between 3 and 4 rib heights, in agreement with results from the literature. These values were also confirmed by flow visualization tests (tufts and surface film tests). The *HTC* distribution for a plate with $p/e = 5$ suggested a single vortex or recirculating region between ribs. The friction factor on the test plates was 5–10 times greater than for the smooth surface.

The local *HTC* distribution (in the similarity region) surrounding the square ribs on the plate with $p/e = 12$ showed that, on the top surface of the rib, a maximum *HTC* occurred at the middle of the rib. This distribution suggested a flow pattern of separation–reattachment–separation over the rib. On the plate with $p/e = 5$, the maximum *HTC* on the top surfaces of the rib occurred at the upstream corner and decreased monotonically downstream, suggesting a pattern of boundary layer growth. The local and average *HTC* values showed that the back surface of the ribs in the test plates had the lowest *HTC* values. The increasing trend from bottom to top of the rib in the local *HTC* distributions of the front and back surfaces of the ribs suggested the existence of recirculation regions at the base of the ribs. An increase in *Re*, and e/D_h caused an increase in the local and average *HTC* on the regions of the test plates.

REFERENCES

1. E. M. Sparrow and W. Q. Tao, Enhanced heat transfer in a flat rectangular duct with streamwise-periodic disturbances at one principal wall, *ASME J. Heat Transfer* **105,** 851–861 (1983).
2. J. C. Han, Heat transfer and friction in channels with two opposite rib-roughened walls, *ASME J. Heat Transfer* **106,** 774–781 (1984).
3. J. C. Han, S. Ou, J. S. Park and C. K. Lei, Heat transfer enhancement in channels with turbulence promoters, *ASME J. Engng Gas Turbines Power* **107,** 628–635 (1985).
4. T. M. Liou, Y. Chang and J. J. Hwang, Experimental and computational study of turbulent flows in a channel with two pairs of turbulence promoters in tandem, *ASME Trans. J. Fluids Engng* **112,** 302–310 (1990).
5. M. Hishida and K. Takase, Heat transfer coefficient of the ribbed surface, *Proceedings of the ASME/JSME Thermal Engineering Conference*, Vol. 3, pp. 103–110 (1991).
6. T. M. Liou and J. J. Hwang, Turbulent heat transfer augmentation and friction in periodic fully developed channel flows, *J. Heat Transfer* **114,** 56–64 (1992).
7. T. L. Bergman and T. S. Labiosa, Forced-convection heat and mass transfer from complex surfaces, *Int. J. Experimental Heat Transfer* **3,** 83–100 (1990).
8. J. H. Torres, T. A. Springer, A. J. Welch and J. A. Pearce, Limitations of a thermal camera in measuring surface temperature of laser-irradiated tissues, *Lasers in Surgery and Medicine* **10,** 510–523 (1990).
9. Inframetrics, *Model 600L Operation Manual*, Billerica, Massachusetts (1991).
10. D. A. Aliaga, D. E. Klein and J. P. Lamb, Heat transfer measurements on a ribbed surface at constant heat flux using infrared thermography, *Int. J. Experimental Heat Transfer* **6,** 17–34 (1993).
11. D. A. Aliaga, Experimental measurements of local heat transfer coefficients over discrete roughened plates using infrared thermography, Ph.D. Dissertation, University of Texas at Austin, Austin, Texas (1992).
12. D. W. Stallings and R. G. Whetsel, Use of infrared imagery in continuous flow wind tunnels, *Proc. of the SPIE Conference Thermosense V*, Vol. 371, pp. 203–209 (1982).
13. R. S. Figliola and D. E. Beasley, *Theory and Design for Mechanical Measurements*, Chap. 5. Wiley, New York (1991).